Observation of two-dimensional Anderson localisation of ultracold atoms

Donald H. White,[1,2,*] Thomas A. Haase,[1,2,†] Dylan J. Brown,[1,2] Maarten D. Hoogerland,[1,2]
Mojdeh S. Najafabadi,[1,3] John L. Helm,[1,3] Christopher Gies,[4] Daniel Schumayer,[1,3] and David A. W. Hutchinson[1,3]

[1] *Dodd-Walls Centre for Photonic and Quantum Technologies, New Zealand*
[2] *Department of Physics, University of Auckland, Auckland, New Zealand*
[3] *Department of Physics, University of Otago, Dunedin, New Zealand*
[4] *Institut für Theoretische Physik, Universität Bremen, Bremen, Germany*

Anderson localisation —the inhibition of wave propagation in disordered media— is a surprising interference phenomenon which is particularly intriguing in two-dimensional (2D) systems. While an ideal, non-interacting 2D system of infinite size is always localised, the localisation length-scale may be too large to be unmistakably observed in an experiment. In this sense, 2D is a marginal dimension between one-dimension where all states are strongly localised, and three-dimensions where a well-defined localisation-delocalisation phase transition exists. Motivated by the goal of observing and closely studying the quantum interference leading to Anderson localisation in a 2D quantum system, we design a transmission experiment in which ultracold atoms propagate through a custom-shaped disordered channel connecting two reservoirs. This design overcomes many of the technical challenges that have hampered observation in previous works. Our precise control of disorder allows us to tune the localisation length to be shorter than the system size. We observe exponential localisation and demonstrate the presence of strong localisation in a 2D ultracold atom system.

Anderson localisation[1] is a phenomenon resulting from wave interference between multiple propagation paths, and has been observed in a variety of wave systems.[2–18] While it is a single-particle phenomenon, its nature is affected by numerous factors including interparticle interactions,[19,20] dimensionality,[21] time-reversal symmetry,[22] spin-orbit coupling,[23] and the microscopic nature of the disorder.[24] A full understanding of the physics of Anderson localisation demands experimental control of these parameters. Ultracold atoms have proven to be among the cleanest and most controllable of all quantum mechanical systems,[25] and have thus provided a natural avenue for modern experiments on Anderson localisation.

Careful experiments with noninteracting atoms expanding in a waveguide containing optically-generated disorder allowed for unambiguous observation of Anderson localisation[26,27] in 1D. These were followed by experiments demonstrating Anderson localisation in 3D,[28,29] and by studies of the metal-insulator transition.[30]

In parallel to this, experiments with cold atoms in 2D have shown behaviours characteristic of weak localisation.[31–33] However, unambiguous observation of Anderson localisation in 2D real-space cold atom systems has, to our knowledge, not previously been observed. This has been due to two main challenges. First, the localisation length in 2D depends exponentially on the particle energy:[34] for experimentally feasible particle energies, observing localisation requires large systems ($> 100\mu\text{m} \times 100\mu\text{m}$) even for ultracold atoms. The optically disordered potential landscapes must have high optical resolution over the entire domain, because the scatterer size must be smaller than the atomic de Broglie wavelength (equivalently, the spatial Fourier components of disorder must exceed the majority of atomic momenta). Secondly, while optical speckle patterns provide appropriate disorder for 1D and 3D systems, the statistics of optical speckle are problematic in 2D due to the high classical percolation threshold of $0.52V_R$, where V_R is the mean disorder potential strength.[35] Observing Anderson localisation in 2D on reasonable length-scales, therefore, requires relatively strong scattering, and this leads to difficulty in distinguishing localisation effects from classical trapping; low energy particles have the shortest localisation lengths, yet they are also trapped classically by the optical speckle. To this end, Morong and DeMarco suggested the use of randomly positioned point scatterers,[35] which allows for a tuneable percolation threshold based on the amount of disorder, and thus allows for quantum interference effects to be effectively isolated from trapping effects.

In this work we implement point scatterers in a 2D plane by projecting a blue-detuned 532 nm optical pattern shaped by a spatial light modulator (SLM) onto a flat, large-area two-dimensional trap formed from 1064 nm light.[36] The SLM enables any arbitrary potential to be projected onto this plane. We take advantage of this flexibility and project the outline of an additional dumbbell-shaped container consisting of two reservoirs separated by a channel,[37,38] with point scatterer disorder located in the channel. Atoms from a ^{87}Rb Bose–Einstein Condensate (BEC) are loaded into the source reservoir, and propagate through the channel into the drain reservoir. The transmissive nature of this experiment has four main advantages compared to traditional expansion ex-

* Present address: Department of Applied Physics, Waseda University, Shinjuku, Tokyo, Japan
† D. H. W. and T. A. H. contributed equally to this work.

periments with ultracold atoms.[39] Firstly, the fraction of atoms collected in the source and drain reservoirs provides a measurement of the effective resistance of the disordered channel. The measurement of atom number in a finite reservoir provides a larger signal-to-noise ratio than is accessible with an expansion experiment. Secondly, measuring the atom distribution within the channel enables us to identify the onset of strong localisation as the channel density profile becomes exponential. The two complementary measurements, of the resistance and the channel profile, provide rich information on the transport properties of the disordered channel. Thirdly, the transmissive nature of the experiment allows us to arbitrarily change the length and width of the atom container, and thus to observe the atom transport on length scales both shorter and longer than the localisation length ξ. Finally, in a transport experiment the Bose gas is not in thermal equilibrium, which suppresses the formation of a Lifshits glass[40,41] (the mixture of low-energy single-particle localised states could mistakenly be identified as Anderson localisation). With these advantages, we tune between the weak- and strong-localised regimes,[42] and observe Anderson localisation of ultracold atoms in 2D.

Our experimental observations are complemented with a systematic numerical analysis in order to understand the experimental findings in more detail and to support their interpretation. On a fundamental level Anderson localisation is a single-particle phenomenon, therefore, its appearance in a quantum system can be captured by a one-body Schrödinger equation with a potential term, $V_{\rm trap}(\mathbf{r})$, corresponding to the confinement and to the 2D static disorder. However, in the experiment some weak interaction, $V_{\rm int}(\mathbf{r})$, is still present between the particles thus the dynamics is governed by the Gross–Pitaevskii equation[43] (GPE)

$$i\hbar\frac{\partial\psi}{\partial t} = \left[-\frac{\hbar^2}{2m}\nabla^2_{\rm 2D} + V_{\rm trap}(\mathbf{r}) + V_{\rm int}(\mathbf{r})\right]\psi, \qquad (1)$$

which we solve using the adaptive, fourth-order Runge-Kutta-Felberg method.[44] Our numerical simulations give access to all experimentally observed quantities and we present them alongside of the experimental measurements for comparison.

The experimental set-up is illustrated in Fig. 1 and is described in detail in Haase et al..[36] A BEC of ^{87}Rb atoms is initially prepared in a crossed-beam CO_2 laser optical dipole trap and $\sim 1.6\times10^4$ atoms in the $|F=1, m_F=-1\rangle$ state are loaded into a large-area quasi-2D trap. The trap is created by interfering two elliptical beams (1.8 mm-to-8 mm height-to-width ratio), each of 5.0 W of 1064 nm light at an angle of 6°. The resulting light sheets are vertically spaced by 8 μm, while the initial diameter of the three-dimensional BEC is $\sim 2\,\mu$m. This allows the ~ 5 nK atoms to load into a single light sheet, with characteristic trap frequencies of $\nu_x = \nu_y = 1$ Hz, $\nu_z = 800$ Hz. This geometry produces a nearly flat potential in the horizontal dimensions, allowing near-ballistic transport with the exception of a weak long-period in-trap interference fringe.[45]

A custom optical potential, produced with an image of a 1280 × 768 pixel Holoeye LC-R 720 spatial light modulator (SLM) is then projected onto the working plane. The image is generated with blue-detuned 532 nm light, and imaged with an in-vacuum aspheric lens of numerical aperture 0.42 to give a resolution of 0.9 μm. A single SLM pixel has dimensions 20 μm × 20 μm, which with a magnification of 0.036 translates to a dimension of 0.72 μm × 0.72 μm in the image plane. The setup allows any custom potential to be drawn, and we image a dumbbell-shaped boundary of two reservoirs of radius r separated in the x direction and linked by a channel of length L and width w. The channel contains customizable, point-like, optical disorder, produced by images of randomly located blocks of 2 × 2 SLM pixels. In the image plane these manifest as approximately Gaussian potential hills of full-width-at-half-maximum $\sigma = 1.4\,\mu$m and 5 nK amplitude.

Atoms are loaded at the centre of the source reservoir and propagate through the channel into the drain reservoir for an expansion time t after the CO_2 laser crossed-beam trap is released. At point of loading, the atoms have a temperature of 5 nK corresponding to a thermal

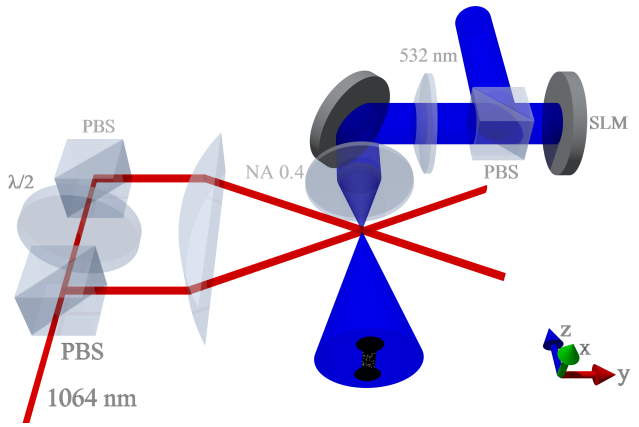

FIG. 1. **Experimental setup.** The two-dimensional trap is produced by interfering two 1064 nm beams, focused with a 250 mm focal length cylindrical lens. The beams intersect at a relative angle of 6° producing horizontal pancake-like interference fringes in the vacuum chamber where the BEC is prepared in a crossed-beam CO_2 optical dipole trap. Atoms from the BEC are loaded into a single light sheet. Simultaneously, a wide and uniform beam of blue-detuned 532 nm light (top right) is reflected from the spatial light modulator (SLM), with a dumbbell-shaped mask applied. Disorder is located within the channel connecting the two reservoirs of the dumbbell. The polarising beamsplitter (PBS) converts the spatial polarisation modulation of the SLM to intensity modulation, which is imaged onto the atomic plane using two lenses. The in-vacuum aspheric lens of numerical aperture 0.42 provides a resolution of 0.9 μm. An example of the combined red and blue optical potentials at the atomic plane are shown in the expanded bottom right bubble.

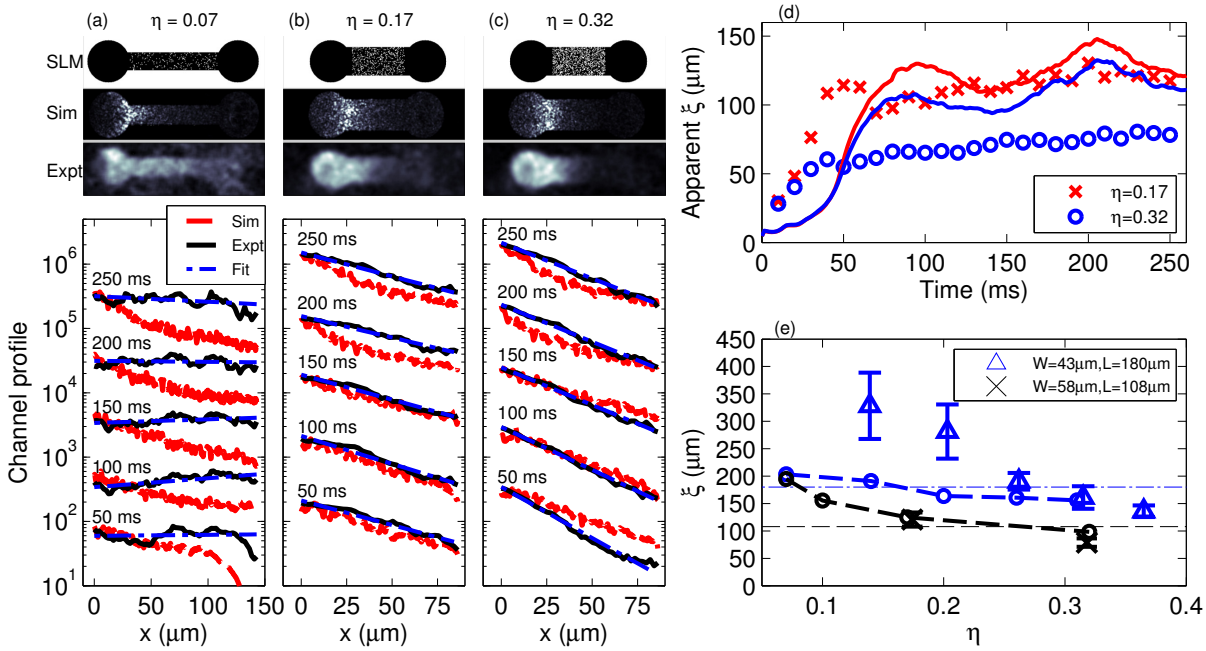

FIG. 2. **Observation of exponential channel density profiles.** (a-c) The top images in each column show the mask applied to the spatial light modulator (white indicates bright pixels). The second row of images shows the density obtained from Gross–Pitaevskii simulations after 250 ms. The third row of images show an average of three experimental absorption images after 250 ms of evolution, each with different disorder realisations. The channel density profiles show semi-logarithmic snapshots of the channel density (in units of atoms per 2.1 μm camera pixel length), at times (50, 100, 150, 200, 250) ms of time evolution, with the density integrated across the y-direction. Each increasing-time snapshot is offset for clarity by a factor of 10. Profiles are overlaid with an exponential fit to the data in blue, and with the density profiles from the GPE simulation in red. Details of the geometry are: (a) $\eta = 0.07$, $(r, L, w) = (43, 180, 36)\,\mu$m; (b) $\eta = 0.17$, $(r, L, w) = (43, 108, 58)\,\mu$m; (c) $\eta = 0.32$, $(r, L, w) = (43, 108, 58)\,\mu$m. (d) The apparent localisation length is found at each time evolution from the weighted exponential fit to the channel profile for two values of η, with $(r, L, w) = (43, 108, 58)\,\mu$m. Results from GPE simulations are shown as solid lines. (e) The localisation length is found as an average of apparent localisation lengths for times 210–250 ms, for two channel geometries. Numerical simulation data is also plotted (joined circles). Errorbars show standard deviations obtained from three trials with different disorder realisations. Dotted lines indicate the channel lengths of 180 μm and 108 μm of the two different geometries. Note that the experimental data for $w = 58$ μm is shown for $\eta = 0.17$ and $\eta = 0.32$ only.

de Broglie wavelength of $\sim 2.6\,\mu$m. The disorder correlation length is approximately half of the de Broglie wavelength, giving the wave scattering properties which allow for Anderson localisation, especially for atoms with energies lower than the mean energy.

Once the atoms have been loaded into the 2D trap, they are left to expand through the channel into the second reservoir. We impart a weak slope to the trap, giving a gravitational acceleration of $\sim 0.002\,\mathrm{m/s^2}$ along the longitudinal direction and thereby atoms acquire $\sim 0.6 k_B T$ of kinetic energy while crossing a 150 μm channel. This linear potential assists the transport by compensating for a weak fringing barrier[45] at the opening of the source reservoir and it is analogous to a weak voltage applied to an electronic thin film in order to obtain a resistance measurement. For sufficiently weak bias, Anderson localisation is expected to be maintained.[46] Data acquisition is performed by capturing absorption images at different expansion times within the dumbbell, in steps of 10 ms up to 250 ms. Example absorption images are shown in the 'Expt' panels of Fig.2a-c. For each fill-factor the experiment is repeated three times, each time with a different disorder realisation to perform configurational averaging.

The disorder is characterised by its fill-factor η, defined as: $\eta = A_{\mathrm{disorder}}/A_{\mathrm{channel}} = n\sigma^2$, where n is the density of scatterers and $\sigma = 1.4\,\mu$m is the effective scatterer width. Equivalently, η is the fraction of bright pixels within the channel displayed by the SLM. Note that the classical percolation threshold of point scatterer disorder is negligible for $\eta \lesssim 0.06$ and remains below that of the optical speckle up to $\eta \lesssim 0.35$.[35]

We quantify transport properties in two ways. First, we analyse the long-time behaviour of the atomic density profile within the channel, which allows direct observation of the presence of Anderson localisation. Second, we measure the temporal behaviour of the source, channel and drain populations (N_s, N_c, N_d). This facilitates the measurement of the transmission coefficient of the channel, which we interpret as a channel 'resistance'.[37]

We first analyse the long-time behaviour of the system. The signature of Anderson localisation is an ex-

ponentially decaying wavefunction, such that the density decays in space with a localisation length of ξ, as:

$$\rho(x) = \rho_0 e^{-2x/\xi}. \quad (2)$$

After many scattering events, the density within the disordered channel should evolve to exhibit an exponentially decaying profile in an Anderson-localised system. Note that 2D is a special case: although there is a Thomas–Fermi distribution of atomic momenta, and therefore a distribution of localisation lengths, the density profile is expected to be exponential.[47] This is a consequence of the finite (yet possibly large) localisation length for all momenta in 2D.

Figures 2a-c plot the time evolution of the channel density profile for three different fill-factors. For weak disorder, we observe a near constant density profile at short evolution times, which evolves to a non-exponential profile for long times. Highly disordered channels ($\eta \geq 0.17$) show distinctly different behaviour. All evolution times over 50 ms indicate an exponential profile. The apparent localisation length, found from the gradient of $\log(\rho(x))$ curve and plotted in Fig. 2d, approaches an asymptotic value for long expansion times. The solution of the Gross–Pitaevskii equation shows similar behaviour, superimposed with an oscillation about a constant value. We also confirm that the simulations exhibit an exponential channel profile with an asymptotic mean localisation length for very long times ($t > 500$ ms). We extract the localisation length measurement from the mean value for expansion times larger than 200 ms and present the result in Fig. 2e. This data indicates that we achieve a localisation length shorter than the channel length of 180 μm for $\eta > 0.25$, with a similar threshold observed for the shorter and wider channel meeting the criterion for strong Anderson localisation. We find a clear relationship showing a reduced localisation length with increasing fill-factor. Numerical simulations give localisation lengths in quantitative agreement with experiment. We also remark on the slightly stronger localisation observed in the wider 58 μm channel compared to the 43 μm channel; a fuller investigation of the width-dependence of the localisation length is planned for further study.

As a second complementary interpretation, we treat the system as an 'atomtronic' circuit[37] and describe the transport in terms of the atomic current flowing between two reservoirs of capacitance C but impeded by a channel resistance R. The atomic current is defined by the number imbalance between the source and drain reservoirs: $\Delta N = (N_s - N_d)/(N_d + N_s)$. Esslinger and co-workers suggested[48] the phenomenological relation

$$\frac{d\Delta N}{dt} = -\frac{\Delta N}{RC}. \quad (3)$$

The data in Fig. 3a shows the evolution of ΔN for varying fill-factors and for three timescales. In the ballistic period atoms transport across the channel and arrive at the second reservoir. In this first period, the imbalance

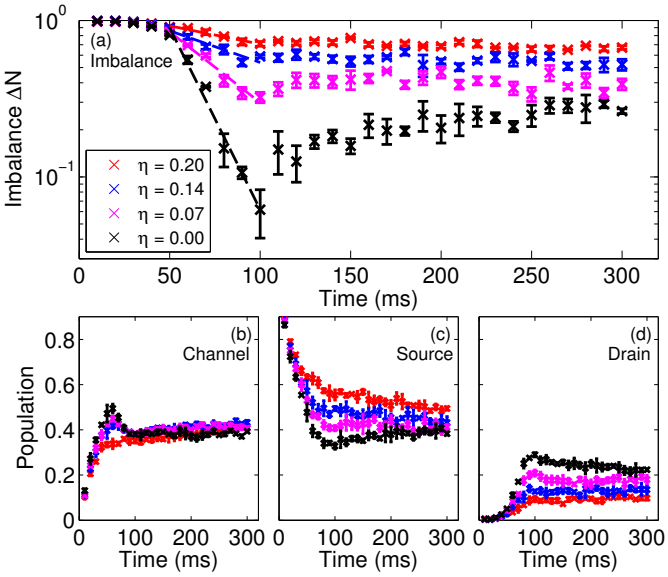

FIG. 3. **Temporal evolution of atom populations.** (a) The number imbalance ΔN vs time for four different fill-factors, with $(r, L, w) = (43, 162, 36)\,\mu$m. Plots are overlaid with the linear fits to the semilogarithmic plot used to calculate the resistance via Eq. (3). (b) Evolution of the channel population. (c) Evolution of the source reservoir population. (d) Evolution of the drain reservoir population.

remains unity due to an empty second reservoir. Following the ballistic time, there is a period of ~ 40 ms during which the imbalance reduces at its greatest rate. This initial transfer rate is greatest for zero disorder. In this period, we find an approximately linear relation between $\log(\Delta N)$ and time, supporting the RC circuit model (3), and we use this transport period to measure the channel resistance. Finally, the system moves into a third regime of transport, in which the number imbalance approaches a steady-state, non-zero value for finite η. This steady-state behaviour is supported by our numerical GPE simulations. We interpret this non-zero steady state number imbalance to be a consequence of a combination of Anderson localisation, and classical trapping for atoms below the percolation threshold when $\eta \gtrsim 0.2$. We note that disorder with low fill-factor (e.g., $\eta = 0.07$) significantly reduces transport, as evidenced by the non-zero steady-state imbalance, although strong Anderson localisation is not observed in this case (cf. Fig. 2a). The reduction in transport is a significant observation, due to the near-zero percolation threshold of $\eta = 0.07$ disorder.[35] In Fig. 3(b-d) we show the populations of the channel and source and drain reservoirs as a function of time. It is apparent that the channel population at longer times does not depend on the fill-factor, whereas the source and drain reservoir populations do. Furthermore, the populations approach a steady state, and the imbalance between the source and the drain increases with increasing η. The steady-state channel population agrees with the relative area of the channel with respect to the whole dumbbell.

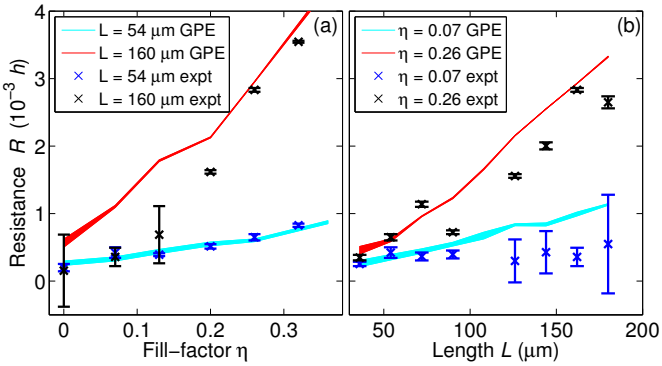

FIG. 4. **Channel resistance measurement.** (a) The resistance as a function of fill-factor, for two channel lengths, in units of Planck's constant. (b) The resistance a function of length, for two fill-factors. Results are overlaid with GPE simulations, with the shaded region indicating one standard-deviation on the simulation value.

The resistance in units of Planck's constant, h, is plotted in Fig. 4 for a range of fill-factors and lengths. In this system, $\hbar C = 19$ s.[45] We observe a stronger dependence of the resistance on fill-factor for longer channel lengths; likewise, we observe a stronger dependence of the resistance on channel length for stronger disorder. While we expect the resistance to be exponential in the channel length in the strongly localised regime,[21] here we observe a slower dependence within the accessible experimental parameters. This is likely due to a significant contribution to the resistance measurement from atoms with energies larger than the mean energy, which have very large localisation lengths. We note close agreement between the experimental data and numerical simulations for the resistance measurements.

In conclusion, we have observed clear signatures of Anderson localisation of atoms in a disordered 2D potential of point scatterers in a regime of weak atomic interaction. Combining a highly tuneable experimental platform with a full numerical GPE simulation, we have observed evidence of Anderson localisation of atoms traversing a disorder potential. The most conclusive experimental and numerical sign of the onset of Anderson localisation is the exponential channel profiles observed for $\eta \geq 0.17$. The logarithm of these profiles are linear and do not change significantly for $t > 100$ ms. We have extracted localisation lengths, ξ, and demonstrated that the transport may be tuned via the disorder fill-factor from a regime of ballistic, to diffusive, and then to strongly localised transport. The dumbbell-shaped architecture enabled two complementary analyses, allowing measurements of the channel resistance, together with the in-channel density evolution. The channel resistance indicates that while atoms traversing weak disorder ($\eta = 0.07$) do not exhibit Anderson localisation, the transport is significantly reduced from the zero-disorder case, despite the near-zero percolation threshold. All experimental observations are supported quantitatively by zero-temperature Gross-Pitaevskii calculations. The support of numerical simulations indicates that Anderson localisation is the suitable interpretation of the exponential density profiles and of the reduced transport. We note that this is the first observation known to us of Anderson localisation in 2D ultracold atom systems. Our work demonstrated and explored the phenomenon of Anderson localisation in a 2D ultracold atomic system. These results provide a springboard for studying localisation and the causes of delocalisation in 2D systems with a quantum-simulator-like device.

[1] P. W. Anderson, Phys. Rev. **109**, 1492 (1958).
[2] M. Cutler and N. F. Mott, Phys. Rev. **181**, 1336 (1969).
[3] P. A. Lee and T. V. Ramakrishnan, Rev. Mod. Phys. **57**, 287 (1985).
[4] R. L. Weaver, Wave Motion **12**, 129 (1990).
[5] R. Dalichaouch, J. P. Armstrong, S. Schultz, P. M. Platzman, and S. L. McCall, Nature **354**, 53 (1991).
[6] D. S. Wiersma, P. Bartolini, A. Lagendijk, and R. Righini, Nature **390**, 671 (1997).
[7] M. Stoytchev and A. Z. Genack, Phys. Rev. B **55**, R8617 (1997).
[8] C. Dembowski, H.-D. Gräf, R. Hofferbert, H. Rehfeld, A. Richter, and T. Weiland, Phys. Rev. E **60**, 3942 (1999).
[9] M. Störzer, P. Gross, C. M. Aegerter, and G. Maret, Phys. Rev. Lett. **96**, 063904 (2006).
[10] J. Topolancik, B. Ilic, and F. Vollmer, Phys. Rev. Lett. **99**, 253901 (2007).
[11] T. Schwartz, G. Bartal, S. Fishman, and M. Segev, Nature **446**, 52 (2007).
[12] H. Hu, A. Strybulevych, J. H. Page, S. E. Skipetrov, and B. A. van Tiggelen, Nature Physics **4**, 945 (2008).
[13] J. Chabé, G. Lemarié, B. Grémaud, D. Delande, P. Szriftgiser, and J. C. Garreau, Phys. Rev. Lett. **101**, 255702 (2008).
[14] F. Riboli, P. Barthelemy, S. Vignolini, F. Intonti, A. D. Rossi, S. Combrie, and D. S. Wiersma, Opt. Lett. **36**, 127 (2011).
[15] T. Sperling, W. Bührer, C. M. Aegerter, and G. Maret, Nature Photonics **7**, 48 (2012).
[16] M. Lopez, J.-F. Clément, P. Szriftgiser, J. C. Garreau, and D. Delande, Phys. Rev. Lett. **108**, 095701 (2012).
[17] I. Manai, J.-F. Clément, R. Chicireanu, C. Hainaut, J. C. Garreau, P. Szriftgiser, and D. Delande, Phys. Rev. Lett. **115**, 240603 (2015).
[18] T. Ying, Y. Gu, X. Chen, X. Wang, S. Jin, L. Zhao, W. Zhang, and X. Chen, Science Advances **2**, e1501283 (2016).
[19] S. Fishman, Y. Krivolapov, and A. Soffer, Nonlinearity **25**, R53 (2012).
[20] D. L. Shepelyansky, Phys. Rev. Lett. **70**, 1787 (1993).
[21] E. Abrahams, P. W. Anderson, D. C. Licciardello, and

T. V. Ramakrishnan, Phys. Rev. Lett. **42**, 673 (1979).
[22] G. Bergmann, Physics Reports **107**, 1 (1984).
[23] G. Bergman, Phys. Rev. Lett. **48**, 1046 (1982).
[24] M. Piraud, A. Aspect, and L. Sanchez-Palencia, Phys. Rev. A **85**, 063611 (2012).
[25] I. M. Georgescu, S. Ashhab, and F. Nori, Rev. Mod. Phys. **86**, 153 (2014).
[26] J. Billy, V. Josse, Z. Zuo, A. Bernard, B. Hambrecht, P. Lugan, D. Clément, L. Sanchez-Palencia, P. Bouyer, and A. Aspect, Nature **453**, 891 (2008).
[27] G. Roati, C. D'Errico, L. Fallani, M. Fattori, C. Fort, M. Zaccanti, G. Modugno, M. Modugno, and M. Inguscio, Nature **453**, 895 (2008).
[28] S. S. Kondov, W. R. McGehee, J. J. Zirbel, and B. DeMarco, Science **334**, 66 (2011).
[29] F. Jendrzejewski, A. Bernard, K. Müller, P. Cheinet, V. Josse, M. Piraud, L. Pezzé, L. Sanchez-Palencia, and P. Aspect, A. Bouyer, Nature Physics **8**, 398 (2011).
[30] G. Semeghini, M. Landini, P. Castilho, S. Roy, G. Spagnolli, A. Trenkwalder, M. Fattori, M. Inguscio, and G. Modugno, Nature Physics **11**, 554 (2015).
[31] M. Robert-de Saint-Vincent, J.-P. Brantut, B. Allard, T. Plisson, L. Pezzé, L. Sanchez-Palencia, A. Aspect, T. Bourdel, and P. Bouyer, Phys. Rev. Lett. **104**, 220602 (2010).
[32] F. Jendrzejewski, K. Müller, J. Richard, A. Date, T. Plisson, P. Bouyer, A. Aspect, and V. Josse, Phys. Rev. Lett. **109**, 195302 (2012).
[33] K. Müller, J. Richard, V. V. Volchkov, V. Denechaud, P. Bouyer, A. Aspect, and V. Josse, Phys. Rev. Lett. **114**, 205301 (2015).
[34] R. C. Kuhn, C. Miniatura, D. Delande, O. Sigwarth, and C. A. Müller, Phys. Rev. Lett. **95**, 250403 (2005).
[35] W. Morong and B. DeMarco, Phys. Rev. A **92**, 023625 (2015).
[36] T. Haase, D. White, D. Brown, I. Herrera, and M. D. Hoogerland, Review of Scientific Instruments **88**, 113102 (2017).
[37] S. Eckel, J. G. Lee, F. Jendrzejewski, C. J. Lobb, G. K. Campbell, and W. T. Hill, Phys. Rev. A **93**, 063619 (2016).
[38] A. Li, S. Eckel, B. Eller, K. E. Warren, C. W. Clark, and M. Edwards, Phys. Rev. A **94**, 023626 (2016).
[39] L. Sanchez-Palencia, D. Clément, P. Lugan, P. Bouyer, and A. Aspect, New Journal of Physics **10**, 045019 (2008).
[40] I. Lifshits, S. Gredeskul, and L. Pastur, *Introduction to the theory of disordered systems*, A Wiley Interscience publication (Wiley, 1988).
[41] P. Lugan, D. Clément, P. Bouyer, A. Aspect, M. Lewenstein, and L. Sanchez-Palencia, Phys. Rev. Lett. **98**, 170403 (2007).
[42] S.-Y. Hsu and J. M. Valles, Jr., Phys. Rev. Lett. **74**, 2331 (1995).
[43] C. Pethick and H. Smith, *Bose-Einstein Condensation in Dilute Gases* (Cambridge University Press, 2002).
[44] R. Burden and J. Faires, *Numerical Analysis* (Brooks/Cole, Cengage Learning, 2011).
[45] Please refer to the supplementary material for further information.
[46] C. Crosnier de Bellaistre, A. Aspect, A. Georges, and L. Sanchez-Palencia, Phys. Rev. B **95**, 140201 (2017).
[47] C. Miniatura, R. C. Kuhn, D. Delande, and C. A. Müller, Eur. Phys. J. B **68**, 353 (2009).
[48] J.-P. Brantut, J. Meineke, D. Stadler, S. Krinner, and T. Esslinger, Science **337**, 1069 (2012).
[49] W. Bao and Q. Du, SIAM J. Sci. Comput. **25**, 1674 (2004).
[50] W. Magnus, Communications on Pure and Applied Mathematics **7**, 649 (1954).

Acknowledgements

The authors would like to thank A. V. H. McPhail and I. Herrera for laboratory assistance. D. H. W. thanks L. Sanchez-Palencia and D. Delande for discussions. C. G would like to thank the German Academic Exchange Service (DAAD) for financial support during his stay at the University of Otago. This work was supported by the Marsden Fund, grant number UOA1330, administered by the Royal Society of New Zealand.

Author Contributions

M. D. H. and D. H. W. planned the research. T. A. H., D. H. W., and D. J. B. constructed the experiment. T. A. H. performed the measurements, with D. J. B. and D. H. W. providing assistance. D. J. B. carried out the data analysis. J. H. wrote the Gross-Pitaevskii code. M. S. N. and D. S ran and analysed the simulations, and together with C. G and D. A. W. H. formed the theoretical underpinning. M. D. H. and D. A. W. H. supervised the experimental and theoretical work, respectively. All authors discussed the research and contributed to the manuscript.

Competing Interests

The authors declare no competing financial interests.

Data availability.

All data presented in this publication is available upon request.

Correspondence

Correspondence and requests for materials related to the experiment can be addressed to Maarten D. Hoogerland (`m.hoogerland@auckland.ac.nz`), while queries regarding the theoretical investigation may be directed to David A. W. Hutchinson (`david.hutchinson@otago.ac.nz`).

I. SUPPLEMENTARY MATERIAL

Here we provide additional experimental details that are of direct relevance to results described in the main text.

A. Experimental details

This experiment has been designed to be a 'quantum simulator' of 2D transport physics. This requires full knowledge of the topography of the 2D potential landscape. Ideally, the basic 2D trap would be flat, with disorder and boundaries introduced by the SLM-projected landscape. While we approximate this condition, we have found the presence of 'fringes' within the 2D trap. These fringes run along the y-direction, and have a period of ≈ 150 μm. The fringe depth is on the order of 5 nK. We attribute the fringes to the interference within the 1064 nm beams, which occurs from distortion to the phase-front of the beam from the vacuum window. The fringe central position may be adjusted by relative horizontal alignment of the two interfering 1064 nm beams, and we set the fringe centre to overlap the centre of the source reservoir.

A linear slope, with acceleration 0.002 m/s, is applied to the 2D trap, meaning that atoms are no longer bound by the fringe, and may enter the trap. While the presence of the fringe affects the bulk motion of the atoms within the channel, the period of the fringe is larger than the channel lengths used, and this means that the Anderson localisation physics should be unchanged. We note close agreement with GPE simulations (discussed below), even if the fringe pattern is excluded.

The BEC is placed such that its centre lies about half way between the centre of the source reservoir and the channel opening. We calibrate the acceleration by adjusting the tilt such that the first wave of atoms arrives at the far end of the drain reservoir at 100 ms after releasing the atoms from the dipole trap, using a 144 μm long channel.

B. Reservoir capacitance

The channel resistance is found from the initial flow of atoms into the drain reservoir, according to

$$\frac{d\Delta N}{dt} = -\frac{\Delta N}{RC}$$

with the reservoir capacitance given by[38]

$$C = \frac{3\left(\frac{1}{2}N\right)^{1/3}}{4\alpha},$$

the constant α is

$$\alpha = \left[\frac{g\left(\frac{1}{2}m\omega_z^2\right)^{1/2}}{\frac{4}{3}\pi r^2}\right]^{2/3},$$

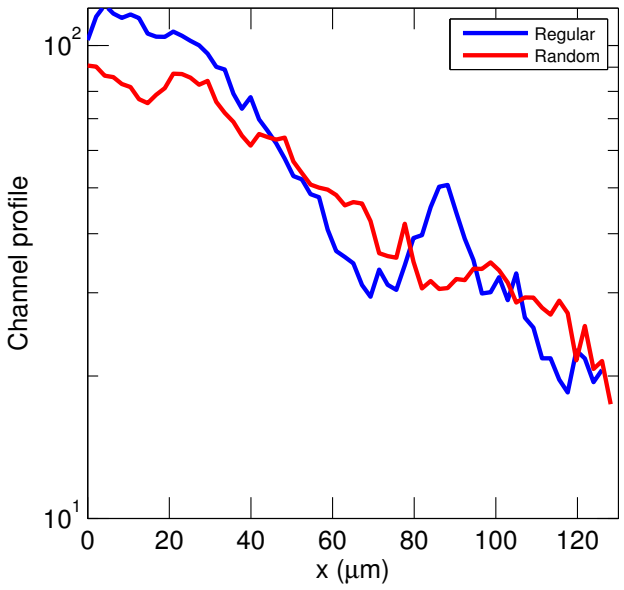

FIG. 5. **Long-time density profile in regular and random lattices** The density at fill-factor $\eta = 0.13$ is shown for scatterers arranged randomly, compared with scatterers arranged in a square regular lattice.

and $g = 4\pi\hbar^2 a_s/m$ is the 3D nonlinearity, r is the reservoir radius, m is the mass of an atom, N is the number of atoms, and ω_z is the vertical trapping frequency. In our system with $r = 43\,\mu$m, $\hbar C = 19\,$s.

C. Comparison between ordered and disordered scatterers

As further evidence that the exponential profile is due to Anderson localisation, we use the tuneability of the spatial light modulator to compare a disordered system with an ordered system. In Fig. 5, we compare the experimental density profiles obtained when the same number of point scatterers ($\eta = 0.13$) are arranged randomly, compared to in a regular ordered square lattice. We observe stronger linearity in the semilogarithmic plot for the disordered case, indicative that the exponential density profile is not due to absence of classical percolation through the optical potential. The semilogarithmic R^2 value of the profile in the regular channel is 0.90, compared with 0.95 of the disordered channel. We also point out the curvature observed in the first 20 μm in the case of regular scatterers. The increased exponential character of a disordered lattice is also found in the simulation. A full study of the comparison between regularly arranged and random scatterers is currently in preparation.

Name	Symbol	Value
particle number	N	16000
^{87}Rb mass	m	$87 \times$ amu
Trap frequency (x)	ω_x	$2\pi \times 1$ rad/s
Trap frequency (y)	ω_y	$2\pi \times 1$ rad/s
Trap frequency (z)	ω_z	$2\pi \times 800$ rad/s
angular frequency of initial trap	ω_0	$2\pi \times 25$ rad/s
s-wave scattering length	a_s	$107a_0$
nonlinearity length	λ	$2\sqrt{2\pi}\,Na_s$
angle of effective gravity	θ	0.0002°
potential depth	$V_{\rm db}$	22 nK
scatterer strength	$V_{\rm sc}$	5 nK

TABLE I. Physical parameters in the numerical simulation.

D. Numerical simulation

Below we provide the values of physical and numerical parameters used in the simulation. We solve the Gross-Pitaevskii equation

$$i\hbar\,\frac{\partial\psi(\mathbf{r},t)}{\partial t} = \left[-\frac{\hbar^2}{2m}\nabla^2_{\rm 2D} + V_{\rm trap}(\mathbf{r},t) + V_{\rm int}(\mathbf{r},t)\right]\psi(\mathbf{r},t)$$

with initial condition $\psi(\mathbf{r},t) = \psi_0(\mathbf{r})$. Here $V_{\rm int}(\mathbf{r})$ denotes the interaction potential

$$V_{\rm int}(\mathbf{r}) = gN\,|\psi(\mathbf{r})|^2 = \frac{2\sqrt{2\pi}\,\hbar^2 a_s}{ma_z}\,N\,|\psi(\mathbf{r})|^2\,,$$

with a_s being the s-wave scattering length of the ^{87}Rb atoms, a_z is the oscillator length of the harmonic oscillator corresponding to ω_z. The trapping potential, $V_{\rm trap}(\mathbf{r})$, includes the strong dumbbell-shaped well of average depth $V_{\rm db}$, the artificial gravitational potential and a weak harmonic potential with minimum at the centre of the dumbbell. We also note here that the presence of the linear tilt causing the artificial gravitational potential, and of the weak harmonic trap in the numerical simulation are included in the calculations for consistency with the experimental setup. The interference fringes due to distortion of the 1064 nm beam wavefront within the 2D trap are not modelled.

Name	Symbol	Value
Spatial extension of the numerical grid in the x direction	L_x	$500\,\mu$m
Spatial extension of the numerical grid in the y direction	L_y	$225\,\mu$m
Number of grid points in the x direction	n_x	1536
Number of grid points in the y direction	n_y	768

TABLE II. Parameters for the numerical simulation.

The initial wavefunction is the ground-state wavefunction of N interacting particles in a three-dimensional harmonic potential with angular frequencies ω_0. This ground-state wavefunction, $\psi_0(\mathbf{r})$, is determined by the standard imaginary-time propagation method,[49,50] and is shifted to the source reservoir. In most of the simulation its centre is located at the opening of the channel. However, we note that the exact position does not strongly influence the transport properties, and only moderately affect the timing. Using the adaptive, fourth-order Runge-Kutta-Felberg method[44] we propagate this initial wavefunction (reduced to a 2D wavefunction) in real time over a grid of size $n_x \times n_y$ representing the rectangular area $L_x \times L_y$ in real space. The dumbbell –for any channel length and circular reservoir radius– is positioned at the centre of this grid symmetrically, i.e, the centre of the channel is at the centre of the numerical grid.

E. Relationship between $\ell_{\rm s}$ and $\ell_{\rm tr}$

The elastic mean free-path between scattering events is approximately given by the mean spacing between scatterers $\ell_{\rm s} = \sigma/\sqrt{\eta}$, while the transport mean free path, $\ell_{\rm tr}$, also known as the Boltzmann mean free path, is the distance over which the memory of the initial direction is lost. It is found[34,45] that $\ell_{\rm tr} = \Lambda(k\sigma)\ell_{\rm s}$, with a proportionality constant Λ dependent on relative size of a scatterer σ and wavelength $\lambda \sim 1/k$. Using the thermal de Broglie wavevector $k_{\rm dB}$ for our experimental setup we obtain $k_{\rm dB}\sigma \approx 3.4$, which translates to $\Lambda(3.4) \approx 40$. We emphasise that there is a Thomas–Fermi distribution of atomic energies in our sample and that Λ depends strongly on $k\sigma$.

First let us determine few characteristic quantities derived from classical or semi-classical approximations. One length scale is provided by the de Broglie wavelength of ^{87}Rb atoms at temperature $T = 5$ nK:

$$\lambda_{\rm dB} = \sqrt{\frac{2\pi\hbar^2}{mk_BT}} \approx 2.65\,\mu{\rm m} \qquad (4)$$

from which the wavenumber is $k_{\rm dB} \approx 2.37 \times 10^6$ m. The physical system also possesses other characteristic length scales: the length of the disordered channel $L_0 \approx 36 - 180\,\mu$m, the channel width $w \approx 14 - 87\,\mu$m, and the mean minimal distance between scatterers $\ell_{\rm sc} \propto \sigma/\sqrt{\eta} \approx 1.7 - 10.2\,\mu$m for the corresponding fill-factors $\eta = 0.8$ and 0.02, respectively. Finally, the smallest length scale defined by the potential is the linear size of a single scatterer, $\sigma \approx 1.44\,\mu$m. In general, therefore, their relationship in the sequence of our experimental runs is $\sigma \lesssim \ell_{\rm sc} < \ell_{\rm tr} < W \lesssim L_0$.

As for length scales, there are also some characteristic energy scales of this system which are given below as temperatures. Furthermore for all length scales we may associate an energy scale as well via energy $\propto \hbar^2/m(\text{length})^2$. We estimated the condensate temperature to be $T_{\rm BEC} \approx 5$ nK, and the BEC is released in a dumbbell-shaped potential with depth of $T_{\rm pot} \approx 22$ nK. The random scatter-

ers have a strength of $T_{\rm sc} \approx T_{\rm pot} \approx 5\,{\rm nK}$. Out of these energy scales we note here the highest which corresponds to σ, the shortest length scale: $E_\sigma = \hbar^2/m\sigma^2 \approx 2.7\,{\rm nK}$.

The scattering process also has a decisive parameter, $k\sigma$, i.e., the relative size of the matter-wave compared to a single scatterer. Using the approximation, $k \approx k_{\rm dB}$, one obtains $k_{\rm dB}\sigma \approx 3.4$. Such value of $k\sigma$ suggests a non-isotropic scattering process even though we are still in the weak scattering regime since the atoms kinetic energies are higher than $E_{\rm sc} = \eta E_\sigma$ for all η values.

In order to establish a relationship between $\ell_{\rm tr}$ and $\ell_{\rm s}$ we evaluate Eq. (6) in Ref.[34]

$$\frac{1}{\Lambda(k\sigma)} = \frac{\ell_{\rm sc}}{\ell_{\rm tr}} = 1 - \frac{\int_0^{2\pi} \cos(\theta)\mathcal{P}(k\sigma,\theta)d\theta}{\int_0^{2\pi} \mathcal{P}(k\sigma,\theta)d\theta} \qquad (5)$$

where $\mathcal{P}(k\sigma,\theta) = 8\mathcal{F}(k\sigma\sin(\theta/2))$ and $\mathcal{F}(x) = \left[\arccos(x) - x\sqrt{1-x^2}\right]\Theta(1-x)$, while Θ denotes the Heaviside distribution.

Figure 6 shows the ratio of the two mean free-paths as a function of the dimensionless $k\sigma$. The inset depicts $\mathcal{P}(k\sigma,\theta)$ as a function of θ for three selected values of $k\sigma$. It is apparent that as $k\sigma \to 0^+$ the function $\mathcal{P}$ is more or less constant 4π. In this limit one may utilise that $\mathcal{F}(x) \sim \frac{\pi}{2} - 2x + \frac{1}{3}x^3$ and determines the integrals in Eq. (5) analytically to obtain

$$\frac{\ell_{\rm tr}}{\ell_{\rm sc}} \sim 1 + \frac{8}{3\pi^2}(k\sigma) + \frac{256}{9\pi^4}(k\sigma)^2 \qquad \text{as } (k\sigma) \to 0^+.$$

In the opposite limit, $k\sigma \to \infty$, the Heaviside distribution in $\mathcal{F}$ is non-zero for $0 \le \theta \le 2\arcsin(1/k\sigma) \approx 2/k\sigma$ or $2\pi - 2/k\sigma \le \theta \le 2\pi$. Therefore the bounds of integrals in Eq. (5) are also restricted to these two small intervals. However, the few leading terms in the Taylor expansion of $\mathcal{F}$ are not sufficient to determine the asymptotic behaviour of $\Lambda(k\sigma)$, but one needs to retain all terms in the expansion

$$\mathcal{F}(x) = \frac{\pi}{2} - 2x + \sum_{n=1}^{\infty} \frac{1}{2^{2n-1}(2n-1)(2n+1)}\binom{2n}{n}x^{2n+1}.$$

The leading term of $\Lambda(k\sigma)$ is quadratic, $c_2(k\sigma)^2$, where the explicit expression of c_2 cannot be given in finite terms. Its value is approximately

$$c_2 \cong \frac{4}{3}\,\frac{6\pi - 11}{6\pi - 16} \approx 3.673$$

At the end we may evaluate the analytic first order correction[34] to the Boltzmann diffusion coefficient for an indicative value of the fill-factor, $\eta = 0.06$,

$$\frac{\delta D}{D_{\rm B}} = \frac{2}{\pi}\,\frac{\ln(L_0/\ell_{\rm s})}{k\ell_{\rm tr}} \approx 3.6 \times 10^{-3}.$$

F. Length scale: average minimal distance

In the main part we have introduced a measure for the average minimal distance between impurity pillars, based on a very simplistic geometric argument. Here, we demonstrate the validity of this measure in the context of our experiment. We calculate the average surrounding area an impurity occupies and then, based on this area, a corresponding length scale by assuming that area is a square. It is reasonable to assume that the average distance between these pillars decisively affect the interference between the quantum wave packets. In particular, at the critical abundance of impurities, as localisation occurs in the system, the shorter distances must influence the interference more strongly than the distance between far away impurities.

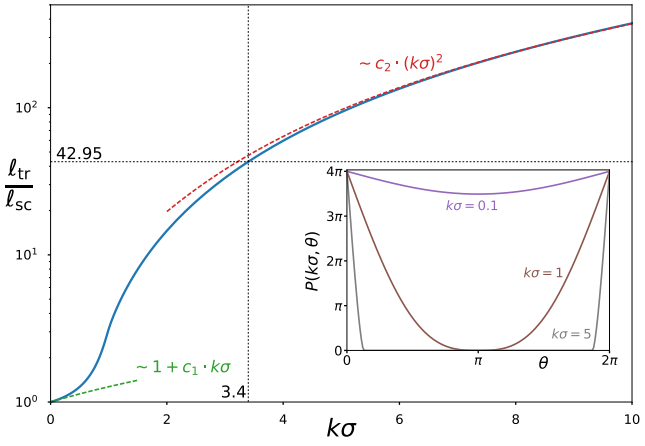

FIG. 6. **Λ as a function of the dimensionless $k\sigma$.** Dashed lines indicate the asymptotic behaviour in both limits, where c_1 and c_2 are constants given in the text. The dotted crosshairs in the main figure correspond to the characteristic value relevant to our experimental setup, $k\sigma = 3.4$. The inset shows the integrand in Eq. (5) dependent as a function of θ for three fixed values $k\sigma = 0.1$, 1 and 5.

$$d_{\rm min} \cong \sqrt{\frac{\text{unoccupied area}}{\text{number of impurities}}} = \sqrt{A_{\rm sc}\left(\frac{1}{\eta} - 1\right)}, \quad (6)$$

where $A_{\rm sc} = 2 \times 2\,{\rm px}^2$. In order to gain a better understanding, we provide an estimate for the footprint of a single pillar.

However, the exact statistics for the minimal distance between neighbouring pillars cannot be deduced from the simplistic geometric argument given in the main text. To confirm that the geometric argument provides a suitable estimate of $d_{\rm min}$ for our experiment, we compare Equation (6) with results obtained from numerical simulation, see Figure 7. 7 depicts the average minimal distance between neighbouring pillars for various values of η. The statistics is gathered from one thousand independent runs for each fixed value of η resulting in the vertical "stripes" in Fig. 7 especially for $\eta < 0.1$. The lower dashed lines represents $d_{\rm min}$ as defined in Eq. (6), while the higher dashed line corresponds to $2d_{\rm min}$. The ratio of the rectangle sides also influence $d_{\rm min}$, thus we have repeated the simulation for all ratios used in the experiment. The overall conclusion is that the discrepancy

between the naive approximation and the exact statistics, especially in the relevant range of $0 < \eta \leq 0.20$, is negligible.

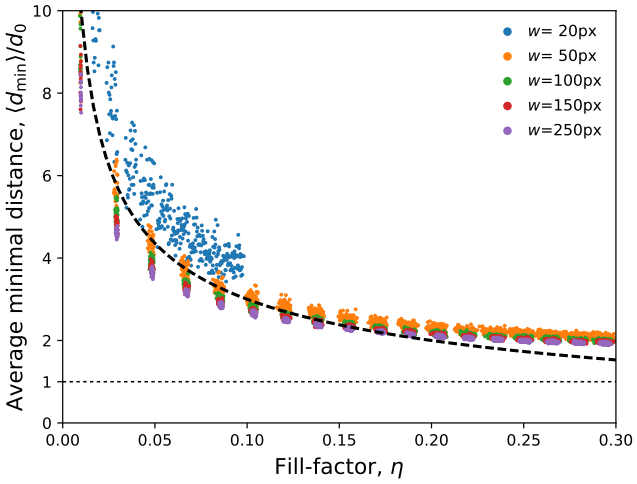

FIG. 7. Comparison of the approximate Eq. (6) (dashed black line) and data extracted from numerical simulations (coloured markers) for the average minimal distance, $\langle d_{\min} \rangle$ as a function of fill-factor, η, and different widths, w. Each value is normalised by d_0. Each marker represents the average minimal distance calculated from a single realisation of disorder. For each η we used 1000 realisations. In all runs $L = 250\,\mathrm{px}$.